The 2018-ongoing Mayotte submarine eruption: Magma migration imaged by petrological monitoring

Carole Berthod, Etienne Médard, Patrick Bachèlery, Lucia Gurioli, Andrea Di Muro, Aline Peltier, Jean-Christophe Komorowski, Mhammed Benbakkar, Jean-Luc Devidal, Jessica Langlade, et al.

The 2018-ongoing Mayotte submarine eruption: magma migration imaged by petrological monitoring

Carole Berthod[(1)*], Etienne Médard[(1)], Patrick Bachèlery[(1)], Lucia Gurioli[(1)], Andrea Di Muro[(2)(3)], Aline Peltier[(2)(3)], Jean-Christophe Komorowski[(3)], Mhammed Benbakkar[(1)], Jean-Luc Devidal[(1)], Jessica Langlade[(4)], Pascale Besson[(3)], Georges Boudon[(3)], Estelle Rose-Koga[(1)], Christine Deplus[(3)], Anne Le Friant[(3)], Manon Bickert[(3)], Sophie Nowak[(3)], Isabelle Thinon[(5)], Pierre Burckel[(3)], Samia Hidalgo[(3)], Melanie Kaliwoda[(6)], Stephan J. Jorry[(7)], Yves Fouquet[(7)], Nathalie Feuillet[(3)]

(1) Université Clermont-Auvergne, CNRS, IRD, OPGC, Laboratoire Magmas et Volcans, 6 avenue Blaise Pascal, 63178 Aubière, France

(2) Observatoire Volcanologique du Piton de la Fournaise, Institut de physique du globe de Paris, F-97418 La Plaine des Cafres, France

(3) Université de Paris, Institut de physique du globe de Paris, CNRS, F-75005 Paris, France

(4) CNRS, Ifremer c/Brest, F-29280 Plouzané, France

(5) BRGM-French geological survey, 3 avenue Claude Guillemin, BP36009, F-45060 Orléans, Cédex 2, France

(6) Ludwig-Maximilians-Universität München, Theresienstrasse 41, D-80333 München, Germany

(6) Ifremer, GM, F-29280 Plouzané, France

Corresponding author: carole.berthod@uca.fr

Highlights

- Lavas erupted offshore Mayotte since May 2018 are evolved basanites (~5 wt% MgO).
- The eruption is fed by a deep (> 37 km) mantle reservoir.
- Primitive magma has undergone at least 50% of crystallization in a ≥ 10 km^3 mantle reservoir.
- Magma transfer rate show that the eruption is steadily supplied from the deep mantle reservoir.
- After May 2019, ascending magma intersected a more evolved and shallower magma reservoir.

Keywords: Mayotte, submarine eruption, dredges, petrological model, mantle reservoirs, multiple storage zone

Abstract

Deep-sea submarine eruptions are the least known type of volcanic activity, due to the difficulty of detecting, monitoring, and sampling them. Following an intense seismic crisis in May 2018, a large submarine effusive eruption offshore the island of Mayotte (Indian Ocean) has extruded at least 6.5 km^3 of magma to date, making it the largest monitored submarine eruption as well as the largest effusive eruption on Earth since Iceland's 1783 Laki eruption. This volcano is located along a WNW-ESE volcanic ridge, extending from the island of Petite Terre (east side of Mayotte) to about 3,500 m of water depth. We present a detailed petrological and geochemical description of the erupted lavas sampled by the MAYOBS 1, 2, and 4 cruises between May and July 2019 and use these to infer characteristics and changes through time for the whole magmatic system and its dynamics from the source to the surface. These cruises provide an exceptional time-series of bathymetric, textural, petrological, and geochemical data for the 2018-2019 eruptive period, and hence bring an invaluable opportunity to better constrain the evolution of magma storage and transfer processes during a long-lived submarine eruption. Integrating the petrological signatures of dredged lavas with geophysical data, we show that the crystal-poor and gas-rich evolved basanitic magma was stored at mantle depth (> 37 km) in a large (≥ 10 km^3) reservoir and that the eruption was tectonically triggered. As the eruption proceeded, a decrease in ascent rate and/or a pathway change resulted in the incorporation of preexisting differentiated magma stored at a shallower level. Magma transfer from the deep mantle reservoir is syn-eruptive, as indicated by transfer times estimated from diffusion in zoned olivine crystals that are much shorter than the total eruption duration. Our petrological model has important hazard implications concerning the rapid and stealthy awakening of a deep gas-rich magma reservoirs that can produce unusually high output rates and long-lived eruption.

Sudden tapping of large crystal poor reservoirs may be the trigger mechanism for other rarely witnessed high-volume (> 1 km^3) effusive events.

1. INTRODUCTION

The discovery in May 2019 of an active volcanic submarine edifice of exceptional size 50 km east of Mayotte island (Comoros Archipelago, Mozambique Channel, Fig. 1a) caused an immediate mobilization of the French scientific community (Feuillet et al., 2019), and the creation of the Mayotte Volcanological and Seismological Monitoring Network (ReVoSiMa, 2021). The eruptive site is located on the distal part of a 60 km long WNW-ESE volcanic ridge that runs off the eastern flank of Mayotte, the subaerial expression of which is Petite Terre Island (Fig. 1b). As of October 2020, this volcano had risen 820 m above the 3300 m deep seafloor with an erupted lava volume of ~ 6.5 km^3 (ReVoSiMa, 2021). This volume implies exceptionally high time-averaged magma discharge rates ranging from 150 – 200 m^3/s (first year), decreasing through 70 – 80 m^3/s (May–July 2019) to less than 35 – 45 m^3/s since August 2019 (ReVoSiMa, 2021). As such, it represents by far the largest monitored submarine eruption (Carey et al., 2018; Chadwick et al., 2018, 2016; Clague et al., 2011; Perfit and Chadwick, 1998; Resing et al., 2011; Rubin et al., 2012) and the third largest mafic eruption of the last two millennia after Eldgjá in 939 (Oppenheimer et al., 2018) and Laki in 1783-1784 (Thordarson and Self, 1993), both in Iceland.

The seismo-volcanic crisis began in May 2018 with a series of strong tectonic earthquakes, including 32 events with $M_W \geq 5$, located between 12 and 42 km depth, ~35 km east of Mayotte (Cesca et al., 2020; Lemoine et al., 2020). On land, surface deformation

(subsidence and eastern motion) have been continuously observed since July 2018, and Very Long Period (VLP) seismic events related to fluid migration and possible magmatic activity have been occurring at least since mid-June 2018 (Cesca et al., 2020; Lemoine et al., 2020), suggesting that the eruptive activity has been ongoing for more than two years. On-going subsidence and seismicity have been linked to the eruption-related withdrawal of magma from its storage zone (Cesca et al., 2020; Feuillet et al., 2020; Lemoine et al., 2020).

Three oceanographic cruises (MAYOBS 1, Feuillet, (2019), MAYOBS 2, Jorry, (2019), MAYOBS 4, Fouquet and Feuillet (2019), Fig. 1c, d) between May and July 2019 provide an exceptional time-series of bathymetric, textural, petrological, and geochemical data for the 2018-2019 eruptive period (Table 1). Since most mafic submarine eruptions are short-lived and have only been sampled after the end of the eruption, their study provides little information on their temporal evolution (Chadwick et al., 2018; Clague et al., 2018; Rubin et al., 2012). The geographically and temporally well-characterized sampling performed during the MAYOBS cruises thus brings an invaluable opportunity to better constrain the evolution of magma storage and transfer during a long-lived submarine eruption. In this paper, we present a detailed petrological, textural, and geochemical study of the submarine samples, to provide insights into the temporal and spatial evolution of a large volume of gas-rich magma rapidly intruding the lithosphere and reactivating multiple levels of magma storage. This is the first time that this methodology, developed for subaerial eruption at monitored volcanoes (Di Muro et al., 2014; Edmonds et al., 2013; Gansecki et al., 2019; Gurioli et al., 2018), and combining a large range of petrological and geochemical approaches on a temporal series of lava samples, is applied to a submarine eruption.

2. GEOLOGICAL SETTING

The Comoros Archipelago is located in the Mozambique Channel between the northern tip of Madagascar and the eastern coast of Mozambique (Fig. 1a). The four islands which compose the archipelago, Grande Comore, Moheli, Anjouan and Mayotte, are aligned on a NW-SE trend (Tzevahirtzian et al., 2020). This trend is superimposed on a zone of active seismicity connecting the northern extremity of Madagascar on the east, to the African coast to the west, and several authors suggest the presence of a boundary between the Lwandle microplate and the Somalia plate (Famin et al., 2020; Saria et al., 2014; Stamps et al., 2018). By combining a structural study with stress inversion of earthquake focal mechanisms, Famin et al. (2020) propose that this Lwandle and Somalian plate boundary is related to a complex E-W zone of immature right-lateral wrenching of the lithosphere.

Despite numerous studies, the origin of the volcanism in this geodynamic context remains a matter of debate (Bachèlery and Hémond, 2016; Class et al., 1998; Claude-Ivanaj et al., 1998; Coltorti et al., 1999; Deniel, 1998; Flower, 1973; Michon, 2016; Nougier et al., 1986; Pelleter et al., 2014; Strong, 1972; Thompson and Flower, 1971). Many hypotheses have been formulated including the interaction of a mantle plume with oceanic lithosphere (Class et al., 1998, 2005, 2009; Claude-Ivanaj et al., 1998; Emerick and Duncan, 1982; Hajash and Armstrong, 1972) and the reactivation of lithospheric structures possibly in relation with the East African Rift System (Lemoine et al., 2020; Michon, 2016; Nougier et al., 1986).

Trace elements and EM1 – HIMU isotopic signatures of volcanic rocks in the Comoros Archipelago would support the interaction of a mantle plume with amphibole/phlogopite-bearing oceanic metasomatized lithosphere (Bachèlery and Hémond, 2016; Class et al., 1998; Pelleter et al., 2014; Späth et al., 1996). However, the mantle plume hypothesis is considered incompatible with the migration of the African Plate towards the NNE and with the structural

features of the region (Famin et al., 2020). Finally, since the youngest volcanic activity occurs both in Grande Comore (0.13 ± 0.02 Ma to present; Hajash and Armstrong, 1972; Emerick and Duncan, 1982) with the active Karthala volcano (Bachèlery et al., 2016) and in Mayotte (Cesca et al., 2020; Feuillet et al., 2020; Lemoine et al., 2020; Zinke et al., 2003), the age progression of volcanism is not consistent with formation of the archipelago by the migration of the Somali plate over a fixed hotspot. Several lines of evidence suggest that the volcanism of the Comoros archipelago is associated with lithospheric deformation rather than the result of a deep mantle plume (Famin et al., 2020; Lemoine et al., 2020; Michon, 2016).

Mayotte, the easternmost island of the archipelago, southwestward of Anjouan (Fig. 1a), is the oldest island with a maximum age of 20 Ma for the onset of subaqueous volcanic activity (Debeuf, 2004; Emerick and Duncan, 1982; Hajash and Armstrong, 1972; Michon, 2016; Nougier et al., 1986; Pelleter et al., 2014). It is composed of two main volcanic islands, Grande Terre and Petite Terre, the latter located 4 km east of Grande Terre. Mayotte subaerial activity is subdivided into multiple phases beginning in the southern part of Grande Terre (10.6 – 1.9 Ma) and then migrating towards the north (5 – 0.75 Ma) and the northeast (0.75 – Present) separated by periods of quiescence (Debeuf, 2004; Nehlig et al., 2013; Pelleter et al., 2014). The current volcanic activity takes place 50 km off Mayotte, on a WNW-ESE submarine volcanic ridge on the east flank of the island, Fig. 1b, (Cesca et al., 2020; Feuillet et al., 2020; Lemoine et al., 2020).

3. METHODS

3.1. Sampling

We first performed a high-resolution bathymetric survey of the eruptive site (Feuillet et al., 2019, 2021) to identify strategic dredging sites. Erupted lavas were dredged on five sites, each dredge running for about 100 – 600 m and returning a weight of approximately 300 – 900 kg (Fig. 1c). During three oceanographic campaigns (MAYOBS 1, Feuillet, (2019), MAYOBS 2, Jorry, (2019), MAYOBS 4, Fouquet and Feuillet (2019)), three dredges sampled the main volcanic cone and the radiating ridges built before May 2019 (phase 1: DR01, DR10, DR12, Table 1 and Fig. 1c, d), and two dredges on the S and SE flanks collected lava flows emitted during a second phase in June 2019 (DR08) and July 2019 (DR11). We selected fresh samples with representative morphologies and textures, including quenched pillow rims, pillow cores, sediments, samples containing xenoliths and phenocrysts. For this paper, we focused our study on glassy pillow rims that preserved the pre-quench textures, as well as xenoliths and phenocryst-rich fragments.

3.2. Analytical techniques

Bulk rock compositions were obtained on a set of 10 samples from 5 dredges (DR0101, DR0105, DR0801-ALF, DR080102, DR100511, DR11, DR1107(1), DR1107(2), DR110704-b and DR120202, Suppl. material Table 1). Major elements were analyzed on a HORIBA-Jobin-Yvon ULTIMA C ICP-AES at Laboratoire Magmas et Volcans (LMV, Clermont-Ferrand, France). Trace elements were analyzed on an Agilent 7900 ICP-MS at Institut de Physique du Globe de Paris (IPGP, Paris, France). In situ chemical analyses of minerals and glasses were performed using the CAMECA SXFive Tactis electron microprobe at LMV. Raman spectra were acquired on melt inclusions in olivine and magnetite, and on matrix glasses at the Ludwig Maximilian University (LMU – Laboratory of crystallography) using an XPlora

One spectrometer (Jobin Yvon) coupled with an Olympus microscope at 100x magnification. Details of the analytical procedures are presented in Supplementary Material "Methods".

3.3. Physical properties and textures

Density measurements were performed on 27 lava samples using a Micromeritics Geopyc 1360 envelope density analyzer, following the procedure detailed by Thivet et al. (2020). The instrument measures the volume of particles with different sizes and shapes. These density measurements lead to reproducible data with a maximum standard deviation of ± 30 $kg.m^{-3}$ (1σ) on five repeated measurements. The porosity of the samples was then calculated using vesicle-free rock density values (Houghton and Wilson, 1989) calculated from the partial molar volumes of oxide components (Bottinga and Weill, 1970). Petrographic observations and microtexture analysis were performed using optical microscope and scan. Vesicle and crystal size distribution (VSD and CSD), vesicle and crystal number density (NV and NC), and vesicle to melt ratio (VG/VL) were measured following the procedures in Shea et al. (2010) and assuming a spherical shape for both vesicles and crystals (mostly olivine).

3.4. Fractional crystallization model

Back-crystallization models were performed to reconstruct a potential mantle-derived parental melt. Equilibrium olivine and clinopyroxene were added in 1 wt % increments to the bulk composition of sample DR0101 until the melt was in equilibrium with a Fo_{90} mantle olivine. For each step, the composition of the equilibrium olivine was calculated from the magma composition of the previous step assuming a Kd of 0.30 ($Kd = (FeO/MgO)_{olivine} / (FeO/MgO)_{melt,}$ Roeder and Emslie, (1970)) and a partition coefficient $D_{Ni} = (Ni^{olivine} / Ni^{melt} = 124 / MgO - 0.9$, Hart and Davis, (1978)). The composition of the equilibrium clinopyroxene was calculated assuming a Kd of 0.28 (Putirka, 2008), oxides vs Mg# trends derived from a series of unpublished clinopyroxene analyses in basanite samples from Mayotte (Hassen Ali,

208 2020), and D_{Ni} = 2. The proportions of olivine and clinopyroxene were adjusted to fit the trend
209 provided by a compilation of published bulk rock analyses from the Comoros Archipelago.

210 *3.5. Diffusion modelling*

211 Preliminary residence times were estimated using diffusion in zoned olivine crystals,
212 modelled with the DIPRA software (Girona and Costa, 2013). Reversely zoned olivine crystals
213 were oriented using an EBSD detector attached to a Zeiss Supra 55 VP field-emission scanning
214 electron microscope housed at ISTeP (Paris, France). Electron microprobe analyses were
215 acquired along carefully selected profiles: we chose olivine crystals most likely to be cut close
216 to their center (large homogeneous core), and the shortest possible profiles, perpendicular to
217 euhedral faces and far from other faces, to avoid artificial lengthening of the profiles (e.g., Costa
218 et al. 2008, Couperthwaite et al. 2021). Fo profiles (Fo = atomic
219 Mg/(Mg+Fe+Mn+Ca+Ni)*100) were modelled using an average temperature of 1095 ± 20 °C,
220 an oxygen fugacity on the NNO buffer, and an arbitrary pressure of 200 MPa. Influence of
221 pressure on diffusion times is within uncertainty.

222

223 **4. RESULTS**

224

225 **4.1. Petrological and geochemical features**

226 Bulk rock compositions of the lavas from the eruptive site fall within the compositional
227 range of the moderately to slightly alkaline series of the Comoros archipelago, the "Karthala
228 trend" (Bachèlery and Hémond, 2016; Class et al., 1998; Claude-Ivanaj et al., 1998; Coltorti et
229 al., 1999; Deniel, 1998; Flower, 1973; Nougier et al., 1986; Pelleter et al., 2014; Strong, 1972;
230 Thompson and Flower, 1971). They are silica-poor (46 < SiO_2 wt.% < 48, Fig. 2a and Suppl.

material Table 1), and plot in the tephrite / basanite field of the TAS classification diagram. Since their normative olivine content is > 10 % they will be referred to as basanites in this study, although they are significantly evolved (4.4 < MgO wt.% < 5.3), and different from mantle-derived primitive basanites. Phase 2 lavas (DR08, DR11) are slightly more evolved than the earliest erupted ones with MgO content spanning a narrow range from 4.4 – 4.6 wt.%. All lavas analyzed are enriched in REE and other incompatible elements and display a steep chondrite-normalized REE pattern, close to the upper range found in the older subaerial Mayotte lavas (Fig. 2c).

Quenched samples are glassy, crystal-poor (4-6% crystals, Figs 3, 4, and Suppl. material Tables 2 and 3), and contain significant amounts of vesicle-trapped volatiles ("popping rocks"). The average vesicularity of lavas is high, 35%, with a maximum of 43%, for phase 1 products (DR01-DR10-DR12) collected on the ridges radiating from the main edifice. Phase 2 lavas, collected on lava flows, are denser (average vesicularity of 31% for DR08, down to 18% for DR11). Except for DR11, these values are much higher than vesicularities of typical MORB popping rocks (Chavrit et al., 2014, 2012), but comparable with the few values measured for submarine alkali basalts. The average vesicularity for all investigated samples is 27 %. Using this average value, the 6.5 km^3 of the new volcano are equivalent to 4.8 km^3 of dense rock. Two binary images of lava fragments from the two textural endmembers (the most and the least vesicular lava) are shown in Fig. 3. DR0103a1 (Fig. 3b) from phase 1, is highly vesicular (43%) and characterized by a homogeneous population of rounded vesicles with a mean size of 0.4 mm. The sample has a relatively high number of vesicles per unit of liquid (Nv, 17 mm^{-3}). In contrast, DR110704b (Fig. 3a) is characterized by a lower vesicularity than DR01, with big, coalesced vesicles, up to 3 mm in diameter and a mean value of 0.8 mm and a drastic decrease in small vesicles, that translate in a low Nv (0.1 mm^{-3}). A general decrease in number of vesicles is evident between the lava samples from phase 1 (DR01-DR10-DR12) and those from phase

256 2 (DR08-DR11), with DR11 samples being the lowest in terms of vesicularity and hence
257 inferred pre-eruptive gas content (Fig. 3c).

258 Crystals in all samples include coeval Fe-rich olivine (50 – 790 μm, $Fo_{69-73.5}$), Ti-
259 magnetite (50 – 100 μm), and apatite (< 20 μm, Fig. 4a, b). Rounded FeS droplets either
260 included in olivine and magnetite crystals or directly in the glass indicate the presence of
261 an immiscible sulphide liquid in some of the samples. Most crystals are euhedral, but skeletal
262 crystals of olivine and titanomagnetite (Fig. 4b) are present in all samples, providing evidence
263 for fast growth, likely linked to fast ascent rates. The small population of olivine phenocrysts,
264 > 0.4 mm (for phase 1 samples) and > 1 mm (for phase 2 samples), represents a very low
265 fraction of the total crystal population (0.3 – 1% of all olivine crystals). In samples from phase
266 2 (June 2019 – July 2019, samples DR08 and DR11), some of the olivine phenocrysts are
267 reversely zoned (Fo_{53} in the cores to Fo_{70} in the rims, Fig. 4c). Their rim composition is similar
268 to that of olivine microlites (Fig. 4a, b).

269 The June 2019 lava flow (sample DR080205) contains small mantle xenoliths (Fig. 4d,
270 e). The largest one (DR080205-x4) is ~5 mm in diameter, and composed of ~1 mm long crystals
271 of Fo_{90} olivine and orthopyroxene with a Mg# (atomic (Mg/(Mg+Fe))*100) of ~90 (Fig. 4d).
272 Some of the orthopyroxene crystals contain clinopyroxene exsolutions. This xenolith also
273 contains veins of SiO_2- and K_2O-rich silicate melts, typical of the melts produced by low-degree
274 melting of phlogopite-bearing mantle (Condamine and Médard 2014). These melt veins are
275 associated with small (< 100 μm) clinopyroxene crystals with Mg# between 92 and 94. A
276 second and smaller xenolith (DR080205-x1), 2.5 mm long (Fig. 4e), is mostly composed of a
277 single clinopyroxene crystal with orthopyroxene exsolutions, and small included crystals of
278 olivine and orthopyroxene. Mineral compositions are similar to those in the first xenolith. A
279 third investigated xenolith (DR080205-x3), only 2 mm in diameter, is similar to the first one,
280 with mostly olivine and orthopyroxene crystals, and clinopyroxene exsolutions in the

orthopyroxene. All xenoliths reacted with the surrounding melts: pyroxene crystals react to form a fine-grained corona of clinopyroxene, olivine, and Ti-magnetite, while olivine crystals are overgrown by an Fo_{72} olivine rim (Fig. 4d, e).

Sample DR080205 also contains a few clinopyroxene megacrysts (Fig. 4f). These megacrysts have a magmatic origin and show an inner, normally zoned core (Mg# 68– 61), surrounded by a more magnesian rim (Mg# 68 – 78). This magnesian rim shows evidence of dissolution and is in turn surrounded by an outer rim made of dendritic clinopyroxene crystals with interstitial glass (Fig. 4f).

Quantification of dissolved water has been performed by micro-Raman spectroscopy in melt inclusions hosted by olivine and titanomagnetite crystals. The pre-eruptive water content is constrained to a minimum of 2.3 wt. % for DR01 and 1.2 wt. % for DR08 (Fig. 5). Our preliminary data suggest that open embayments can retain high water contents comparable to those of the closed melt inclusions, suggesting the occurrence of disequilibrium water degassing during magma ascent. Disequilibrium water degassing typically results from fast magma ascent. It can be favored by the low crystal content, and in turn can delay melt crystallization and bubble nucleation (Ferguson et al., 2016; Lloyd et al., 2014).

4.2. Thermobarometry

Pre-eruptive temperatures for the main erupted magmas were calculated using the olivine-melt equilibrium and the equations of Beattie (1993) and Ford et al. (1983). Equilibrium olivine-glass pairs were selected based on a Fe/Mg Kd of 0.30 ± 0.05, assuming a Fe^{3+}/Fe_{total} ratio of 0.15, and the temperatures were averaged on 3 – 14 couples per sample. For thermometry calculations, the pressure was arbitrarily set at 200 MPa, however, the influence of pressure is limited to a few degrees per 100 MPa. Results from the model of Beattie (1993),

and from the T_{sum} equation of Ford et al. (1983) are within 2 – 8 °C of each other. Anhydrous calculated temperatures were corrected for the effect of H_2O using average H_2O concentration determined by micro-Raman spectrometry and the olivine liquidus depression model of Médard and Grove (2008). Uncorrected pre-eruptive temperatures are 1151 ± 20 °C for phase 1 (DR01-DR10-DR12) and 1136 ± 20 °C for phase 2 (DR08-DR11). Corrected temperatures are within error for all samples, at 1095 ± 20 °C. Note that if melt inclusion provides a minimum pre-eruptive water content, this calculation provides a maximum pre-eruptive temperature.

Pre-eruptive temperature and oxygen fugacity for the magma batch parent to the Fo_{55} olivine cores were calculated from an ilmenite-titanomagnetite intergrowth included in Fo_{55} olivine, which constrains magmatic conditions of this evolved batch to 1024 ± 50 °C and an oxygen fugacity (fO_2) close to that of the nickel-nickel oxide buffer (Sauerzapf et al., 2008). Thermometry of melt inclusions in Fo_{52} olivine gives similar anhydrous temperatures of about 1046 ± 20 °C (Beattie, 1993).

We analyzed a series of clinopyroxene-orthopyroxene pairs in the mantle xenoliths (Fig. 4d, e) to obtain pressure and temperature constraints. In xenolith DR080205-x4, we analyzed clinopyroxene-orthopyroxene pairs associated with the high-SiO_2 high-K_2O veins, as well as exsolutions of clinopyroxene in orthopyroxene. In the other two xenoliths, we only analyzed exsolutions, either of orthopyroxene in clinopyroxene (DR080205-x1), or of clinopyroxene in orthopyroxene (DR080205-x3). Temperatures were calculated using equation (36) of Putirka et al. (2008) with reported uncertainties of 45 °C. For pressure, both equations (38) and (39) were tested against experiments performed at 1.00 GPa by Condamine and Médard (2014) on pyroxene in equilibrium with high-SiO_2 high-K_2O veins. Since equation (38) returned an average pressure of 1.02 GPa, whereas equation (39) returned an average pressure of 0.88, Equation (38) was preferred for the calculation. It reproduces the experimental data with an average error (SEE) of 0.19 GPa. Equilibration pressures for the xenoliths are 0.43 GPa at a

330 temperature of 926 °C for DR080205-x1 (Fig. 6a-c, Suppl. material Table 5), 0.41 GPa at a
331 temperature of 890 °C for DR080205-x3 and 0.46 GPa at a temperature of 913 °C for
332 DR080205-x4. Assuming an average density of 2890 kg m^{-3} for an oceanic crust and 3300 kg
333 m^{-3} for the upper mantle, these xenoliths were equilibrated at an average depth below the sea
334 level of 17 ± 6 km (0.45 ± 0.19 GPa).

335 We made an estimation of the magma storage depth by applying a clinopyroxene- only
336 geobarometer (Equation 32b with water content of 2.3 wt.%, Putirka, 2008) to a zoned
337 clinopyroxene megacryst in sample DR080502-x2 (Fig. 4f). The core of the crystal returns a
338 depth range of 37 to 48 (P = 1.01 – 1.34 GPa). A second cluster with values ranging from 24 to
339 34 (P = 0.62 – 0.92 GPa) is associated with the inner rim. A few low-pressure values (0.14 –
340 0.38 GPa) were obtained on the outer dendritic rim and could indicate crystallization in the
341 conduit during magma ascent (Fig. 6d). Uncertainties associated with these calculations are 10
342 km (0.28 GPa, Putirka 2008). A second analyzed zoned clinopyroxene megacryst generates
343 similar clusters. Phenocrysts in equilibrium with the bulk rock are expected to have Mg# of 75
344 (olivine) and 78 (clinopyroxene), indicating that the most magnesian olivine cores and the
345 clinopyroxene inner rims are in equilibrium with the magma. The more Fe-rich clinopyroxene
346 cores should thus be interpreted as an antecrystic crystal cargo.

347

348 **4.3. Olivine diffusion and residence times**

349 Five different reversely zoned olivine crystals in DR0801-ALF, DR110704 and DR110401
350 samples were investigated (Fig. 7a,b), assuming an initial step function with an olivine core
351 between Fo_{53-60} depending on the crystal, surrounded by an overgrowth rim Fo_{69-70} (Fig. 7b).
352 Two zoned olivine crystals at the edge of an harzburgite xenolith (DR080502x4) were also

353 modelled, using a step function with a Fo_{90} olivine core and a Fo_{72} olivine overgrowth (Fig.
354 7c,d) but without EBSD orientation.

355 The five diffusion profiles in reversely zoned olivine crystals can be modelled with
356 diffusion times of 29 ± 9, 24 ± 8, 19 ± 7, 38 ± 12 and 40 ± 11 days (supplementary material
357 Table 6, errors are given at the two sigma level). Since no EBSD data was acquired in the two
358 normally zoned olivine crystals from xenolith DR080205x4, we can only provide a time bracket
359 using maximum and minimum diffusion coefficient. Thus, these profiles can be modelled with
360 diffusion times between 12 and 69 and between 8 and 47 days. Fits assuming instantaneous
361 growth of the outer rims followed by pure diffusion are excellent with the reversely zoned
362 crystals (supplementary material Table 6), and very good for the xenolith. The assumption of
363 instantaneous crystal growth is supported by the orders of magnitude of difference between
364 crystal growth rates and elemental diffusion rates (e.g., Petrone et al. 2016). These preliminary
365 diffusion times can be interpreted as residence times for the olivine crystals and the xenolith,
366 between injection of the incoming magma in the shallow magma pocket and its eruption at the
367 surface.

368

369 ## 5. DISCUSSION

370

371 ### 5.1. Source

372

373 The magmas erupted during the ongoing Mayotte eruption are evolved basanite that likely
374 derive from more primitive (unerupted) basanitic mantle melts. The low HREE concentrations
375 and the strongly fractionated REE patterns ($(Tb/Yb)_N$ = 2.9 – 3.2, Fig. 2c) indicate the presence
376 of residual garnet in the mantle source. Moreover, Sm/Yb and La/Sm ratios for the erupted

lavas indicate a spinel/garnet lherzolitic source (Fig. 2d). This is consistent with previous studies on subaerial Comoros lavas which suggest that primary magmas are produced by small degrees of partial melting at the depth of the spinel to garnet lherzolite transition, 80 – 100 km (Bachèlery and Hémond, 2016; Class et al., 1998). Furthermore, olivine melilitites in Mayotte volcanic products and evidence of metasomatizing carbonatitic fluids on Grande Comore suggest a CO_2-rich mantle source (Coltorti et al., 1999; Pelleter et al., 2014). The P_2O_5 enrichment of the new volcano samples, together with the high Sr and Ba contents, and high Nb/Yb ratio, are consistent with an apatite contribution in the genesis of these lavas. Presence of a mm-sized apatite xenocryst in one of our lava samples suggests a possible assimilation of apatite-bearing veins during the ascent of primary melts formed at a greater depth, as indicated by Pelleter et al., (2014). Homogeneous P_2O_5 enrichment compared to other Comoros lavas is observed in all of our samples (1. 6 – 2.0 wt.%, Suppl. material Table 1), which precludes a late assimilation and argues for a mantle source origin of the inferred apatite-bearing veins.

5.2. Deep magma reservoir in the lithospheric mantle

The evolved nature (low Mg#, 43 – 47) of the erupted magmas shows that they are not primary products of mantle melting since the expected Mg# of primary mantle melts in equilibrium with Fo_{90} olivine is ~73, assuming an olivine/melt Kd of 0.30 (Roeder and Emslie, 1970). Extensive cooling and crystallization must thus have occurred in a lithospheric magma reservoir (Fig. 8). A back-crystallization model consistent with the general trend of Comoros lavas (Bachèlery and Hémond, 2016; Class et al., 1998; Claude-Ivanaj et al., 1998; Coltorti et al., 1999; Deniel, 1998; Flower, 1973; Nougier et al., 1986; Pelleter et al., 2014; Strong, 1972; Thompson and Flower, 1971) requires approximately 50% crystallization of an olivine-clinopyroxene assemblage (80% clinopyroxene $Mg\#_{91\text{-}76}$ and 20% olivine $Fo_{90\text{-}75}$) to reproduce

401 the erupted magma compositions (Fig. 2b). This implies that the reservoir, where mantle-
402 derived magma is ponding and differentiating, has a volume of at least ~10 km^3 (~5 km^3 of
403 erupted magma and the same amount of crystals) and is zoned, with ~ 5 km^3 of residual dense
404 cumulates. This is a minimum reservoir size, since the estimation relies on the unlikely
405 hypothesis that melt and cumulates were perfectly segregated, and does not take into account
406 any interstitial melt within the cumulates and the contribution of deep CO_2 exsolution. The
407 occurrence of a large reservoir is also supported by ratios of intrusive to extrusive volumes
408 commonly estimated at ~5:1 for oceanic mid-ocean ridges (Crisp, 1984; White et al., 2006).
409 Since the erupted magma was a true homogeneous liquid, and the few crystals of the main cone-
410 building phase 1 are unzoned, this suggests the system was not disturbed by new primary
411 magma replenishment and was able to evolve to yield a single well-stratified reservoir. In
412 sample DR080205-x2, clinopyroxene megacryst cores were equilibrated at pressures of 1.01 –
413 1.34 GPa (from Putirka, 2008, equation 32b, i.e. 37 – 48 km, Figs 6d and 8). This provides the
414 depth for the main reservoir feeding the current eruption, which is thus located in the
415 lithospheric mantle, in agreement with seismological and geodetic models (Cesca et al., 2020;
416 Lemoine et al., 2020). The slowly waning effusion rate is also characteristic of an eruption fed
417 by a deep reservoir (Wadge, 1981).

418 Magma ascending from lithospheric mantle storage entrained mantle xenoliths from a
419 shallower depth, near the Moho, at an average depth of 17 ± 6 km. The time between
420 entrainment of the mantle xenoliths and eruption is estimated less than 70 days. Given that the
421 xenoliths were picked up en route to the surface, this is a preliminary estimation of the transfer
422 time between the deep magma reservoir and the eruption site. It is consistent with the 6 weeks
423 of precursory unrest estimated from seismological data (Cesca et al., 2020; Lemoine et al.,
424 2020).

425

5.3. Differentiated shallower magma batch

Phase 1 products are crystal-poor lavas with high density of vesicles (Fig. 3b), skeletal crystals (Fig. 4a, b) and high dissolved water content (Fig. 5). Thus, we suggest that during the first year, eruption is fed by direct ascent of magma from the deep reservoir to the surface. The shape and the size of microlites indicate that most micro-crystallization occurred in the shallow part of the ascending dyke. The degree of magmatic evolution increases from phase 1 to phase 2 lavas (Fig. 1d). This increase is mirrored by a decrease in vesicularity, vesicle number density (Fig. 3) and dissolved water content (Fig. 5), indicating that late erupted lavas were increasingly outgassed. Reverse zoning in olivine phenocrysts from phase 2 lavas (Fig. 4c) records the interaction between the hot basanitic magma, ascending from the ≥ 37 km deep storage zone, and a second cooler magma batch (Fig. 8). Since transfer times estimated from diffusion in those crystals (~ 1 month) are similar to transfer times estimated from the mantle xenoliths, the zoned olivine crystals probably came from a similar or shallower depth than the xenoliths. Pyroxenes in the mantle xenoliths record a depth of 17 ± 6 km, interpreted to represent the maximum depth of this shallower reservoir (Fig. 6). The inner rim in clinopyroxene megacryst (DR080205-x4, Fig. 4f), equilibrated at pressures of 0.8 ± 0.28 GPa (28 ± 10 km), may indicate the location of a third magma storage zone.

Because no seismicity at this shallow depth was detected (ReVoSiMa, 2021), the differentiated magma batch is unlikely to occupy a large dynamic reservoir but rather perhaps magma ponding at the base of the Moho. Analysis of diffusion profiles in reversely zoned olivine from phase 2 lava flows constrain the time between the start of Fo_{70} olivine crystallization and eruption. We obtain minimum estimations of ~ 1 month for the time between mixing with the shallower magma batch and eruption of the hybrid magma (Fig. 7, Suppl. material Table 6). Magma mixing and transfer of hybrid magma thus occurred during the

eruption and were not related to long-term precursor activity detected by the permanent land-based monitoring networks.

5.4. Eruption trigger

The erupted products are evolved alkaline mafic magmas and have a minimum dissolved water content of ca. 2 wt. % (Fig. 5). Available thermodynamic models permit us to crudely estimate the pre-eruptive dissolved CO_2 content as being in the range 0.6 – 1.2 wt % (Allison et al., 2019; Papale et al., 2006). This is compatible with the possible presence of an exsolved CO_2-rich fluid phase in the plumbing system. Under these conditions, the magma chamber will be pressurized, but stable. Because of the deep location and the associated pressure, volume changes due to crystallization or volatile exsolution should not be sufficient to act as an eruption trigger. Moreover, we found no evidence of primitive magma in the erupted products. Therefore, we suggest that fault movement or earthquakes rather than a deep reservoir recharge event was responsible for the sudden initial decompression and fast ascent of a large volume of volatile-rich melt stored in the mantle.

The eruption site belongs to a WNW-ESE volcano-tectonic ridge, parallel to regional trends, suggesting relation to a pre-existing tectonic structure. Deep seismicity recorded during the seismo-volcanic crisis (Cesca et al., 2020; Lemoine et al., 2020; ReVoSiMa, 2021) implies that these structures are deeply rooted in the lithosphere (up to 50 km depth). The sequence of strong tectonic earthquakes recorded at the beginning of the eruption (volcano-tectonic events located at 34 – 41 km depth, 35 km east of Mayotte (Cesca et al., 2020; Lemoine et al., 2020) might thus be related to the movement along the lithospheric faults.

5.5. Syn-eruptive magma path change

Since the melt was volatile-saturated (CO_2+H_2O) in the deep reservoir, magma ascent towards the surface would have resulted in continuous exsolution of CO_2 first and then CO_2+H_2O up to the eruption site. Full exsolution of pre-eruptive dissolved volatiles at the vent would produce a fluid with a molar volume of ca. 320 cm^3/mol and vesicularity in the range 54 – 71 vol%, values much higher than those measured in our samples (Suppl. material Tables 2 and 3). Vesicularity would be even higher if there were additional exsolved CO_2 in the reservoir. Incomplete disequilibrium degassing because of the fast ascent rate and rapid quenching on the seafloor can explain the difference between the expected and measured vesicularities. We also suggest that rapid decompression-induced crystallization (Hammer et al., 1999) in the shallow conduit may be responsible for the skeletal shape of olivine and Ti-magnetite crystals (Faure et al., 2003). The absence of reversely zoned olivine crystals in phase 1 products suggests that basanitic melts ascended from the deep reservoir directly to the surface during the first year of eruption (Fig. 8).

In contrast, the presence of reversely zoned olivine with Fo_{53} cores in phase 2 lava flows (Fig. 4c) indicates that, after May 2019 magma ascending from the deep reservoir intersected a more evolved magma batch, at a depth near the Moho on its way to the surface (Fig. 8). Using a simple mass balance model, we estimate that only 6% of the evolved magma (represented by melt inclusions in Fo_{53} olivine in sample DR11) was assimilated in the erupted lavas, indicating that the intersected volume of this shallower reservoir is much smaller than the deeper one. Less abundant (low Nv) and larger vesicles (Fig. 3) are consistent with a slower ascent and lower volatile content during phase 2. The residual magmatic liquid in the shallower magma batch could have been produced by fractional crystallization from an older magma intrusion, as observed during Kilauea's 2018 eruption (Gansecki et al., 2019). Due to the time required for magmatic differentiation (decades, Gansecki et al., 2019), this observation implies magma

intrusion and possible recent volcanic activity in the offshore part of the volcanic ridge prior to the current eruption. The emission of the more evolved magma in phase 2 could have resulted either from a change in the dyke pathway (as suggested by the presence of mantle xenoliths) and/or a decrease in magma discharge rate allowing the input from the second shallower magma source.

Zoned olivine phenocrysts took ~ 1 month to be transferred from the ~ 17 km shallow reservoir to the seafloor. Thus, we obtain a minimum ascent rate of 0.005 $m.s^{-1}$ from the shallow reservoir to the surface for the slower pathway (Fig. 8).

6. CONCLUSIONS

The large and long-lasting effusive eruption offshore from Mayotte is fed by a deep (> 37 km) and large (≥ 10 km^3) pre-existing mantle reservoir of evolved, alkaline magma that experienced extensive crystallization. This has important volcanic hazard implications, because it demonstrates that this large, volatile-rich deep reservoir could quickly be tapped in a tectonically active region to feed a voluminous and long-lasting effusive eruption. During the eruption, magma ascent slowed and switched to a pathway that sampled a small more chemically evolved shallower magma batch at the base of the crust. Our petrological study provides important constraints on the entire deep magmatic system from the source to the surface. These results bring valuable and critical information complementary to geophysical datasets, showing that we can use the petrology of erupted products for long-term monitoring of extreme events even when they occur in poorly accessible environments. These data helped to determine the geometry and the dynamics of magmatic plumbing systems, and provided critical constraints for the interpretation of geophysical datasets in terms of processes and patterns.

Acknowledgements

MAYOBS 1 campaign was funded by the CNRS-INSU TELLUS MAYOTTE program (SISMAYOTTE project). MAYOBS 1, 2 and 4 campaigns were conducted by several French research institutions and laboratories (IPGP/CNRS/BRGM/IFREMER/IPGS). We want to thank the crew of R/V Marion Dufresne (TAAF/IFREMER/LDA). Analyses were funded by the Service National d'Observation en Volcanologie (SNOV, INSU) and the Réseau de Surveillance Volcanologique et Sismologique de Mayotte (REVOSIMA), a partnership between the Institut de Physique du Globe de Paris (IPGP), the Bureau de Recherches Géologiques et Minières (BRGM), and the Observatoire Volcanologique du Piton de la Fournaise (OVPF-IPGP), the Centre National de la Recherche Scientifique (CNRS), and the Institut Français de Recherche pour l'Exploitation de la Mer (IFREMER). The authors would like to thank Andrew Harris for reviewing and English improvement before submission, IFREMER for their welcome during the sampling and E. Humler for his support and national funding coordination (CNRS, REVOSIMA). Raman data were acquired by ADM as a side project during his fellowship at the Center for Advanced Studies of the Ludwig-Maximilians-Universität München (CAS LMU) in collaboration with the CAS Research Group on "Magma to Tephra: Ash in the Earth System" (Resp. Prof. Donald Dingwell). We thank Ivonne Cocca (Université de Paris) for assistance in sample preparation. Finally, we are also grateful for the helpful reviews provided by William Chadwick, an anonymous reviewer, and editorial handling by Chiara Petrone. This is a Labex ClerVolc contribution number 466.

References

Allison, C.M., Roggensack, K., Clarke, A.B., 2019. H2O–CO2 solubility in alkali-rich mafic magmas: new experiments at mid-crustal pressures. Contrib. Mineral. Petrol. 174, 58. https://doi.org/10.1007/s00410-019-1592-4

Bachèlery, P., Hémond, C., 2016. Geochemical and Petrological Aspects of Karthala Volcano, in: Active Volcanoes of the Southwest Indian Ocean. Springer, pp. 367–384.

Bachèlery, P., Morin, J., Villeneuve, N., Soulé, H., Nassor, H., Ali, A.R., 2016. Structure and eruptive history of Karthala volcano, in: Active Volcanoes of the Southwest Indian Ocean. Springer, pp. 345–366.

Beattie, P., 1993. Olivine-melt and orthopyroxene-melt equilibria. Contrib. Mineral. Petrol. 115, 103–111. https://doi.org/10.1007/BF00712982

Bottinga, Y., Weill, D.F., 1970. Densities of liquid silicate systems calculated from partial molar volumes of oxide components. Am. J. Sci. 269, 169–182.

Carey, R., Soule, S.A., Manga, M., White, J.D.L., McPhie, J., Wysoczanski, R., Jutzeler, M., Tani, K., Yoerger, D., Fornari, D., 2018. The largest deep-ocean silicic volcanic eruption of the past century. Sci. Adv. 4, e1701121. https://doi.org/10.1126/sciadv.1701121

Cesca, S., Letort, J., Razafindrakoto, H.N.T., Heimann, S., Rivalta, E., Isken, M.P., Nikkhoo, M., Passarelli, L., Petersen, G.M., Cotton, F., Dahm, T., 2020. Drainage of a deep magma reservoir near Mayotte inferred from seismicity and deformation. Nat. Geosci. 13, 87–93. https://doi.org/10.1038/s41561-019-0505-5

Chadwick, W.W., Merle, S.G., Baker, E.T., Walker, S.L., Resing, J.A., Butterfield, D.A., Anderson, M.O., Baumberger, T., Bobbitt, A.M., 2018. A recent volcanic eruption discovered on the central Mariana back-arc spreading center. Front. Earth Sci. 6, 172. https://doi.org/10.3389/feart.2018.00172

Chadwick, W.W., Paduan, J.B., Clague, D.A., Dreyer, B.M., Merle, S.G., Bobbitt, A.M., Caress, D.W., Philip, B.T., Kelley, D.S., Nooner, S.L., 2016. Voluminous eruption from a zoned magma body after an increase in supply rate at Axial Seamount. Geophys. Res. Lett. 43, 12063–12070. https://doi.org/10.1002/2016GL071327.

Chavrit, D., Humler, E., Grasset, O., 2014. Mapping modern CO2 fluxes and mantle carbon content all along the mid-ocean ridge system. Earth Planet. Sci. Lett. 387, 229–239. https://doi.org/10.1016/j.epsl.2013.11.036

Chavrit, D., Humler, E., Morizet, Y., Laporte, D., 2012. Influence of magma ascent rate on carbon dioxide degassing at oceanic ridges: Message in a bubble. Earth Planet. Sci. Lett. 357, 376–385. https://doi.org/10.1016/j.epsl.2012.09.042

Clague, D.A., Paduan, J.B., Caress, D.W., Thomas, H., Chadwick Jr, W.W., Merle, S.G., 2011. Volcanic morphology of West Mata Volcano, NE Lau Basin, based on high-resolution bathymetry and depth changes. Geochemistry, Geophys. Geosystems 12. https://doi.org/10.1029/2011GC003791

Clague, D.A., Paduan, J.B., Dreyer, B.M., Chadwick Jr, W.W., Rubin, K.R., Perfit, M.R., Fundis, A.T., 2018. Chemical variations in the 1998, 2011, and 2015 lava flows from Axial Seamount, Juan de Fuca Ridge: Cooling during ascent, lateral transport, and flow. Geochemistry, Geophys. Geosystems 19, 2915–2933. https://doi.org/10.1029/2018GC007708

Class, C., Goldstein, S.L., Altherr, R., Bachèlery, P., 1998. The process of plume–lithosphere interactions in the ocean basins—the case of Grande Comore. J. Petrol. 39, 881–903. https://doi.org/10.1093/petroj/39.5.881

589 Class, C., Goldstein, S.L., Shirey, S.B., 2009. Osmium isotopes in Grande Comore lavas: a new
590 extreme among a spectrum of EM-type mantle endmembers. Earth Planet. Sci. Lett. 284,
591 219–227. https://doi.org/10.1016/j.epsl.2009.04.031

592 Class, C., Goldstein, S.L., Stute, M., Kurz, M.D., Schlosser, P., 2005. Grand Comore Island: A
593 well-constrained "low 3He/4He" mantle plume. Earth Planet. Sci. Lett. 233, 391–409.
594 https://doi.org/10.1016/j.epsl.2005.02.029

595 Claude-Ivanaj, C., Bourdon, B., Allègre, C.J., 1998. Ra–Th–Sr isotope systematics in Grande
596 Comore Island: a case study of plume–lithosphere interaction. Earth Planet. Sci. Lett. 164,
597 99–117. https://doi.org/10.1016/S0012-821X(98)00195-2

598 Coltorti, M., Bonadiman, C., Hinton, R.W., Siena, F., Upton, B.G.J., 1999. Carbonatite
599 metasomatism of the oceanic upper mantle: evidence from clinopyroxenes and glasses in
600 ultramafic xenoliths of Grande Comore, Indian Ocean. J. Petrol. 40, 133–165.
601 https://doi.org/10.1016/j.epsl.2014.04.027

602 Condamine, P., Médard, E., 2014. Experimental melting of phlogopite-bearing mantle at 1 GPa:
603 Implications for potassic magmatism. Earth Planet. Sci. Lett. 397, 80–92.
604 https://doi.org/10.1016/j.epsl.2014.04.027

605 Crisp, J.A., 1984. Rates of magma emplacement and volcanic output. J. Volcanol. Geotherm.
606 Res. 20, 177–211. https://doi.org/10.1016/0377-0273(84)90039-8

607 Costa, F., Dohmen, R., Chakraborty, S., 2008. Time scales of magmatic processes from
608 modeling the zoning patterns of crystals. Rev. Mineral. Geochemistry 69, 545–594.
609 https://doi.org/10.2138/rmg.2008.69.14

610 Couperthwaite, F.K., Morgan, D.J., Pankhurst, M.J., Lee, P.D., Day, J.M.D., 2021. Reducing
611 epistemic and model uncertainty in ionic inter-diffusion chronology: A 3D observation
612 and dynamic modeling approach using olivine from Piton de la Fournaise, La Réunion.
613 Am. Mineral. J. Earth Planet. Mater. 106, 481–494. https://doi.org/10.2138/am-2021-
614 7296CCBY

615 Debeuf, D., 2004. Étude de l'évolution volcano-structurale et magmatique de Mayotte (archipel
616 des Comores, océan Indien). PhD thesis, Université de la Réunion, France.

617 Deniel, C., 1998. Geochemical and isotopic (Sr, Nd, Pb) evidence for plume–lithosphere
618 interactions in the genesis of Grande Comore magmas (Indian Ocean). Chem. Geol. 144,
619 281–303. https://doi.org/10.1016/S0009-2541(97)00139-3

620 Di Muro, A., Métrich, N., Vergani, D., Rosi, M., Armienti, P., Fougeroux, T., Deloule, E.,
621 Arienzo, I., Civetta, L., 2014. The shallow plumbing system of Piton de la Fournaise
622 Volcano (La Reunion Island, Indian Ocean) revealed by the major 2007 caldera-forming
623 eruption. J. Petrol. 55, 1287–1315. https://doi.org/10.1093/petrology/egu025

624 Di Muro, A., Villemant, B., Montagnac, G., Scaillet, B., Reynard, B., 2006. Quantification of
625 water content and speciation in natural silicic glasses (phonolite, dacite, rhyolite) by
626 confocal microRaman spectrometry. Geochim. Cosmochim. Acta 70, 2868–2884.
627 https://doi.org/10.1016/j.gca.2006.02.016

628 Dofal, A., Fontaine, F.R., Michon, L., Barruol, G., Tkalcic, H., 2018. Crustal structure variation
629 across the southwestern Indian Ocean from receiver functions determined at Ocean-
630 Bottom Seismometers, in: AGU Fall Meeting 2018. AGU.

631 Edmonds, M., Sides, I.R., Swanson, D.A., Werner, C., Martin, R.S., Mather, T.A., Herd, R.A.,
632 Jones, R.L., Mead, M.I., Sawyer, G., 2013. Magma storage, transport and degassing during
633 the 2008–10 summit eruption at Kīlauea Volcano, Hawai 'i. Geochim. Cosmochim. Acta
634 123, 284–301. https://doi.org/10.1016/j.gca.2013.05.038

635 Emerick, C.M., Duncan, R.A., 1982. Age progressive volcanism in the Comores Archipelago,
636 western Indian Ocean and implications for Somali plate tectonics. Earth Planet. Sci. Lett.
637 60, 415–428. https://doi.org/10.1016/0012-821X(82)90077-2

638 Famin, V., Michon, L., Bourhane, A., 2020. The Comoros archipelago: a right-lateral transform
639 boundary between the Somalia and Lwandle plates. Tectonophysics 789, 228539.
640 https://doi.org/10.1016/j.tecto.2020.228539

641 Faure, F., Trolliard, G., Nicollet, C., Montel, J.-M., 2003. A developmental model of olivine
642 morphology as a function of the cooling rate and the degree of undercooling. Contrib.
643 Mineral. Petrol. 145, 251–263. https://doi.org/10.1007/s00410-003-0449-y

644 Ferguson, D.J., Gonnermann, H.M., Ruprecht, P., Plank, T., Hauri, E.H., Houghton, B.F.,
645 Swanson, D.A., 2016. Magma decompression rates during explosive eruptions of Kīlauea
646 volcano, Hawaii, recorded by melt embayments. Bull. Volcanol. 78, 71.
647 https://doi.org/10.1007/s00445-016-1064-x

648 Feuillet, N., 2019. MAYOBS1 cruise, RV Marion Dufresne.
649 https://doi.org/10.17600/18001217

650 Feuillet, N., Jorry, S., Rinnert, E., Thinon, I., Fouquet, Y., 2019. MAYOBS cruises, RV Marion
651 Dufresne. https://doi.org/10.18142/291

652 Feuillet, N., Jorry, S.J., Crawford, W., Deplus, C., Thinon, I., Jacques, E., Saurel, J.M.,
653 Lemoine, A., Paquet, F., Satriano, C., Aiken, C., Foix, O., Kowalski, P., Laurent, A.,
654 Rinnert, E., Cathalot, C., Donval, J.P., Guyader, V., Gaillot, A., Scalabrin, C., Moreira,
655 M., Peltier, A., Beauducel, F., Grandin, R., Ballu, V., Daniel, R., Pelleau, P., Gomez, J.,
656 Besançon, S., Geli, L., Bernard, P., Bachèlery, P., Fouquet, Y., Bertil, D., Lemarchand,
657 A., van der Woerd, J., 2020. Birth of a large volcanic edifice through lithosphere-scale
658 diking offshore Mayotte (Indian Ocean). EarthArXiv. https://doi.org/10.31223/X5B89P

659 Flower, M.F.J., 1973. Evolution of basaltic and differentiated lavas from Anjouan, Comores
660 Archipelago. Contrib. to Mineral. Petrol. 38, 237–260.

661 Ford, C.E., Russell, D.G., Craven, J.A., Fisk, M.R., 1983. Olivine-liquid equilibria:
662 temperature, pressure and composition dependence of the crystal/liquid cation partition
663 coefficients for Mg, Fe2+, Ca and Mn. J. Petrol. 24, 256–266.
664 https://doi.org/10.1093/petrology/24.3.256

665 Fouquet, Y., Feuillet, N., 2019. MAYOBS4 cruise, RV Marion Dufresne.
666 https://doi.org/10.17600/18001238

667 Gansecki, C., Lee, R.L., Shea, T., Lundblad, S.P., Hon, K., Parcheta, C., 2019. The tangled tale
668 of Kīlauea's 2018 eruption as told by geochemical monitoring. Science (80-.). 366.
669 https://doi.org/10.1126/science.aaz0147

670 Girona, T., Costa, F., 2013. DIPRA: A user-friendly program to model multi-element diffusion
671 in olivine with applications to timescales of magmatic processes. Geochemistry, Geophys.
672 Geosystems 14, 422–431. https://doi.org/10.1029/2012GC004427

673 Gurioli, L., Di Muro, A., Vlastélic, I., Moune, S., Thivet, S., Valer, M., Villeneuve, N.,
674 Boudoire, G., Peltier, A., Bachèlery, P., 2018. Integrating field, textural, and geochemical
675 monitoring to track eruption triggers and dynamics: a case study from Piton de la
676 Fournaise. Solid Earth 9, 431–455. https://doi.org/10.5194/se-9-431-2018

677 Hajash, A., Armstrong, R.L., 1972. Paleomagnetic and radiometric evidence for the age of the
678 Comores Islands, west central Indian Ocean. Earth Planet. Sci. Lett. 16, 231–236.
679 https://doi.org/10.1016/0012-821X(72)90195-1

680 Hammer, J.E., Cashman, K. V, Hoblitt, R.P., Newman, S., 1999. Degassing and microlite
681 crystallization during pre-climactic events of the 1991 eruption of Mt. Pinatubo,
682 Philippines. Bull. Volcanol. 60, 355–380. https://doi.org/10.1007/s004450050238

683 Hart, S.R., Davis, K.E., 1978. Nickel partitioning between olivine and silicate melt. Earth
684 Planet. Sci. Lett. 40, 203–219.

685 Hassen Ali, T., 2020. Etude pétrochimique du volcanisme récent de Mayotte. Master thesis,
686 Université Clermont Auvergne, Clermont-Ferrand, France.

687 Houghton, B.F., Wilson, C.J.N., 1989. A vesicularity index for pyroclastic deposits. Bull.
688 Volcanol. 51, 451–462. https://doi.org/10.1007/BF01078811

689 Jorry, S.J., 2019. MAYOBS2 cruise, RV Marion Dufresne. https://doi.org/10.17600/18001222

690 Lemoine, A., Briole, P., Bertil, D., Roullé, A., Foumel, M., THINON, I., Raucoules, D.,
691 Michele, M. de, Valty, P., 2020. The 2018-2019 seismo-volcanic crisis east of Mayotte,
692 Comoros islands: seismicity and ground deformation markers of an exceptional submarine
693 eruption. Geophys. J. International 223(1): 22-44. https://doi.org/10.31223/osf.io/d46xj

694 Lloyd, A.S., Ruprecht, P., Hauri, E.H., Rose, W., Gonnermann, H.M., Plank, T., 2014.
695 NanoSIMS results from olivine-hosted melt embayments: magma ascent rate during
696 explosive basaltic eruptions. J. Volcanol. Geotherm. Res. 283, 1–18.
697 https://doi.org/10.1016/j.jvolgeores.2014.06.002

698 Médard, E., Grove, T.L., 2008. The effect of H_2O on the olivine liquidus of basaltic melts:
699 experiments and thermodynamic models. Contrib. Mineral. Petrol. 155, 417–432.
700 https://doi.org/10.1007/s00410-007-0250-4

701 Michon, L., 2016. The volcanism of the Comoros archipelago integrated at a regional scale, in:
702 Active Volcanoes of the Southwest Indian Ocean. Springer, pp. 333–344.
703 https://doi.org/10.1007/978-3-642-31395-0_21

704 Nehlig, P., Lacquement, F., Bernard, J., Caroff, M., Deparis, J., Jaouen, T., Pelleter, A.A.,
705 Perrin, J., Prognon, C., Vittecoq, B., 2013. Notice de la carte géologique de Mayotte.
706 BRGM/RP-61803-FR, 135 p., 45 ill., 1 ann.

707 Nougier, J., Cantagrel, J.M., Karche, J.P., 1986. The Comores archipelago in the western Indian
708 Ocean: volcanology, geochronology and geodynamic setting. J. African Earth Sci. 5, 135–
709 144. https://doi.org/10.1016/0899-5362(86)90003-5

710 Oppenheimer, C., Orchard, A., Stoffel, M., Newfield, T.P., Guillet, S., Corona, C., Sigl, M., Di
711 Cosmo, N., Büntgen, U., 2018. The Eldgjá eruption: timing, long-range impacts and
712 influence on the Christianisation of Iceland. Clim. Change 147, 369–381.
713 https://doi.org/10.1007/s10584-018-2171-9

714 Papale, P., Moretti, R., Barbato, D., 2006. The compositional dependence of the saturation
715 surface of H2O+ CO2 fluids in silicate melts. Chem. Geol. 229, 78–95.
716 https://doi.org/10.1016/j.chemgeo.2006.01.013

717 Patrick, M., Johanson, I., Shea, T., Waite, G., 2020. The historic events at Kīlauea Volcano in
718 2018: summit collapse, rift zone eruption, and Mw 6.9 earthquake: preface to the special
719 issue. Bull. Volcanol. 82, 46. https://doi.org/0.1007/s00445-020-01377-5

720 Pelleter, A.-A., Caroff, M., Cordier, C., Bachèlery, P., Nehlig, P., Debeuf, D., Arnaud, N., 2014.
721 Melilite-bearing lavas in Mayotte (France): An insight into the mantle source below the
722 Comores. Lithos 208, 281–297. https://doi.org/10.1016/j.lithos.2014.09.012

723 Perfit, M.R., Chadwick, W.W., 1998. Magmatism at mid-ocean ridges: Constraints from
724 volcanological and geochemical investigations. Geophys. Monogr. Geophys. Union 106,
725 59–116.

726 Petrone, C.M., Bugatti, G., Braschi, E., Tommasini, S., 2016. Pre-eruptive magmatic processes
727 re-timed using a non-isothermal approach to magma chamber dynamics. Nat. Commun. 7,
728 1–11. https://doi.org/10.1038/ncomms12946

729 Pouclet, A., Bellon, H., Bram, K., 2016. The Cenozoic volcanism in the Kivu rift: Assessment
730 of the tectonic setting, geochemistry, and geochronology of the volcanic activity in the
731 South-Kivu and Virunga regions. J. African Earth Sci. 121, 219–246.
732 https://doi.org/10.1016/j.jafrearsci.2016.05.026

733 Putirka, K.D., 2008. Thermometers and Barometers for Volcanic Systems. Rev. Mineral.
734 Geochemistry 69, 61–120. https://doi.org/10.2138/rmg.2008.69.3

735 Resing, J.A., Rubin, K.H., Embley, R.W., Lupton, J.E., Baker, E.T., Dziak, R.P., Baumberger,
736 T., Lilley, M.D., Huber, J.A., Shank, T.M., 2011. Active submarine eruption of boninite
737 in the northeastern Lau Basin. Nat. Geosci. 4, 799–806. https://doi.org/10.1038/ngeo1275

738 ReVoSiMa, 2021. Bulletin n°21 de l'activité sismo-volcanique à Mayotte, du 1 au 31 janvier
739 2021. ISSN : 2680-1205. https://www.brgm.fr/sites/default/files/documents/2021-
740 02/dossier-thematique-mayotte-bulletin-revosima-026.pdf

741 Roeder, P.L., Emslie, Rf., 1970. Olivine-liquid equilibrium. Contrib. to Mineral. Petrol. 29,
742 275–289.

743 Rubin, K.H., Soule, S.A., Chadwick, W.W., Fornari, D.J., Clague, D.A., Embley, R.W., Baker,
744 E.T., Perfit, M.R., Caress, D.W., Dziak, R.P., 2012. Volcanic eruptions in the deep sea.
745 Oceanography 25, 142–157.

746 Saria, E., Calais, E., Stamps, D.S., Delvaux, D., Hartnady, C.J.H., 2014. Present-day kinematics
747 of the East African Rift. J. Geophys. Res. Solid Earth 119, 3584–3600.
748 https://doi.org/10.1002/2013JB010901

749 Sauerzapf, U., Lattard, D., Burchard, M., Engelmann, R., 2008. The Titanomagnetite - Ilmenite
750 Equilibrium : New Experimental Data and Thermo-oxybarometric Application to the
751 Crystallization of Basic to Intermediate Rocks. J. Petrol. 49, 1161–1185.
752 https://doi.org/10.1093/petrology/egn021

753 Shea, T., Houghton, B.F., Gurioli, L., Cashman, K. V, Hammer, J.E., Hobden, B.J., 2010.
754 Textural studies of vesicles in volcanic rocks: an integrated methodology. J. Volcanol.

Geotherm. Res. 190, 271–289. https://doi.org/10.1016/j.jvolgeores.2009.12.003

Späth, A., Roex, A.P. Le, Duncan, R.A., 1996. The geochemistry of lavas from the Comores Archipelago, Western Indian Ocean: petrogenesis and mantle source region characteristics. J. Petrol. 37, 961–991. https://doi.org/10.1093/petrology/37.4.961

Stamps, D.S., Saria, E., Kreemer, C., 2018. A Geodetic Strain Rate Model for the East African Rift System. Sci. Rep. 8, 732. https://doi.org/10.1038/s41598-017-19097-w

Strong, D.F., 1972. Petrology of the island of Moheli, western Indian Ocean. Geol. Soc. Am. Bull. 83, 389–406.

Thivet, S., Gurioli, L., Di Muro, A., 2020. Basaltic dyke eruptions at Piton de La Fournaise: characterization of the eruptive products with implications for reservoir conditions, conduit processes and eruptive dynamics. Contrib. to Mineral. Petrol. 175, 1–24. https://doi.org/10.1007/s00410-020-1664-5

Thompson, R.N., Flower, M.F.J., 1971. One-atmosphere melting and crystallization relations of lavas from Anjouan, Comores Archipelago, Western Indian Ocean. Earth Planet. Sci. Lett. 12, 97–107. https://doi.org/10.1016/0012-821X(71)90060-4

Thordarson, T., Miller, D.J., Larsen, G., Self, S., Sigurdsson, H., 2001. New estimates of sulfur degassing and atmospheric mass-loading by the 934 AD Eldgjá eruption, Iceland. J. Volcanol. Geotherm. Res. 108, 33–54. https://doi.org/10.1016/S0377-0273(00)00277-8

Thordarson, T., Self, S., 1993. The Laki (Skaftár Fires) and Grímsvötn eruptions in 1783–1785. Bull. Volcanol. 55, 233–263. https://doi.org/10.1007/BF00624353

Tzevahirtzian, A., Zaragosi, S., Bachèlery, P., Biscara, L., Marchès, E., 2020. Submarine morphology of the Comoros volcanic archipelago. Mar. Geol. 432. https://doi.org/10.1016/j.margeo.2020.106383

Wadge, G., 1981. The variation of magma discharge during basaltic eruptions. J. Volcanol. Geotherm. Res. 11, 139–168. https://doi.org/10.1016/0377-0273(81)90020-2

White, S.M., Crisp, J.A., Spera, F.J., 2006. Long-term volumetric eruption rates and magma budgets. Geochemistry, Geophys. Geosystems 7. https://doi.org/10.1029/2005GC001002

Zinke, J., Reijmer, J.J.G., Thomassin, B.A., Dullo, W.-C., Grootes, P.M., Erlenkeuser, H., 2003. Postglacial flooding history of Mayotte lagoon (Comoro archipelago, southwest Indian Ocean). Mar. Geol. 194, 181–196. https://doi.org/10.1016/S0025-3227(02)00705-3

Figure captions

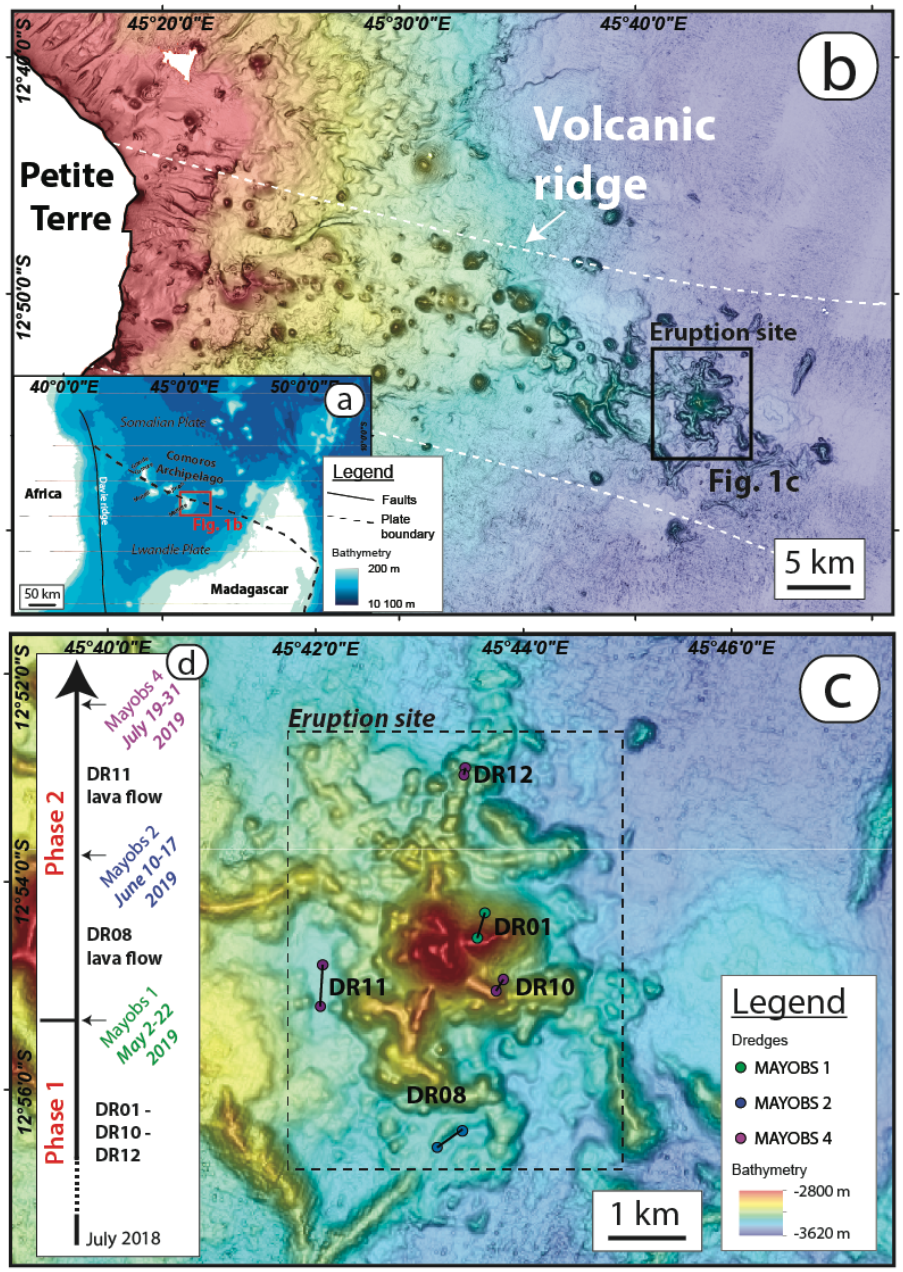

Fig. 1: Location of the eruptive site. a) Comoros volcanic archipelago is located in the northern part of the Mozambique Channel. b) Location of the new volcanic edifice 50 km east of Mayotte along the submarine volcanic ridge crossing Mayotte eastern flank. c) Location of the five dredges (DR) carried out during the three oceanographic campaigns (MAYOBS 1, 2 and 4), superimposed on bathymetric data from the MAYOBS 1 cruise (May 2019). d) Sampling related to eruption timing. DR01, DR10 and DR12 lavas were erupted before May 2019 during

the cone-building phase 1 and sampled by MAYOBS 1 and 4 oceanographic cruises; DR08 and DR11 are lava flows emitted in June and July 2019 (phase 2) and sampled during Mayobs 2 and 4 oceanographic cruises, respectively.

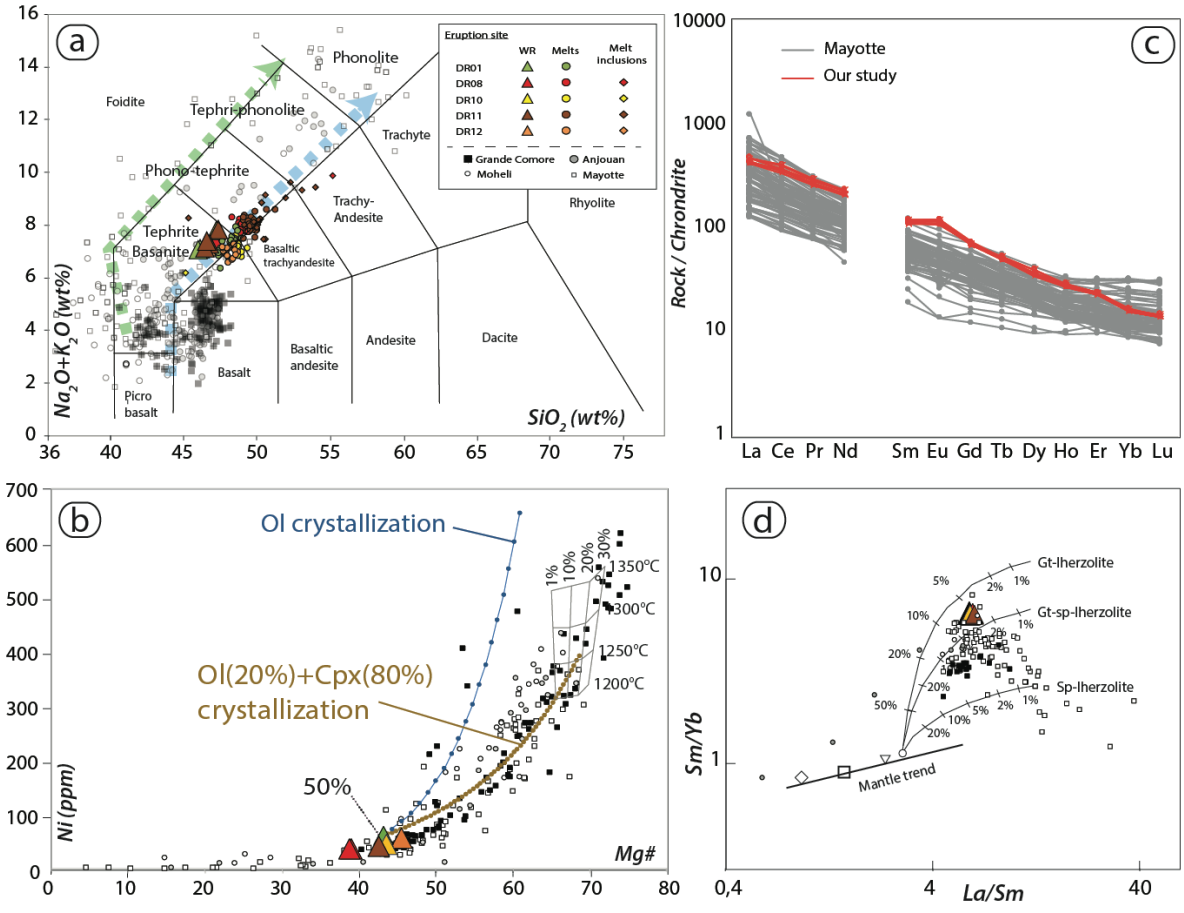

Fig. 2: Bulk rock geochemistry of the dredged evolved basanite lavas emitted during the 2018-2020 Mayotte eruption. a) TAS classification comparing the composition of the submarine lavas of the new edifice (Suppl. material Table 1) with that of subaerial lavas from the Comoros archipelago. Blue and green arrows show the moderately silica-undersaturated ("Karthala-trend") and the highly silica-undersaturated ("La Grille-trend") trends identified in Comoros lavas, respectively. b) Fractional crystallization models for Comoros and Mayotte lavas plotted in Ni (ppm) vs Mg# space. Melts in equilibrium with the mantle have a Mg# ~70 (the melting grid with mantle melting temperature and melt fractions has been computed following Späth et al., 1996)). Back calculation models start from DR0101 composition by adding in small

increments of equilibrium olivine and clinopyroxene compositions appropriate to match the composition of subaerial Comoros lavas and consistent with the Ni concentration for a primary mantle melt (300-500 ppm, Späth et al., (1996)). Olivine-only fractionation fails to reproduce the Comoros trend. c) Chondrite-normalized REE patterns of the submarine lavas of the new edifice compared to Mayotte subaerial lavas. d) La/Sm vs Sm/Yb diagram annotated with partial melting curves for garnet and spinel lherzolite mantle sources (Pouclet et al., 2016).

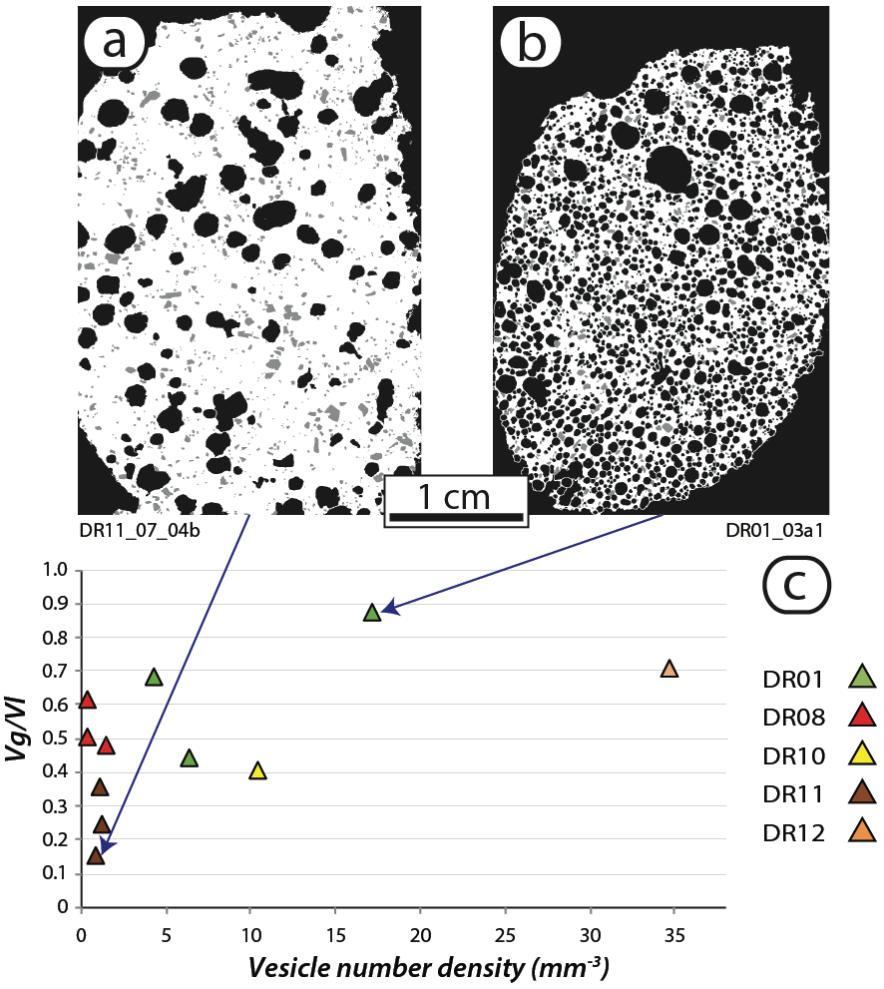

Fig. 3: Textural characteristics of the studied lava samples. Binary images of two lava fragments a) DR110704-b and b) DR0103-a1 where black = vesicles, white = glass and grey = crystals. c) Vesicle to melt ratio (Vg/Vl) vs. vesicle number density. A decrease in vesicle number density (Nv) is evident from the samples from phase 1 (DR01-DR10-DR12) to those

824 from phase 2 (DR08-DR11), with DR11 samples being the lowest in term of vesicularity and
825 inferred pre-eruptive gas content.

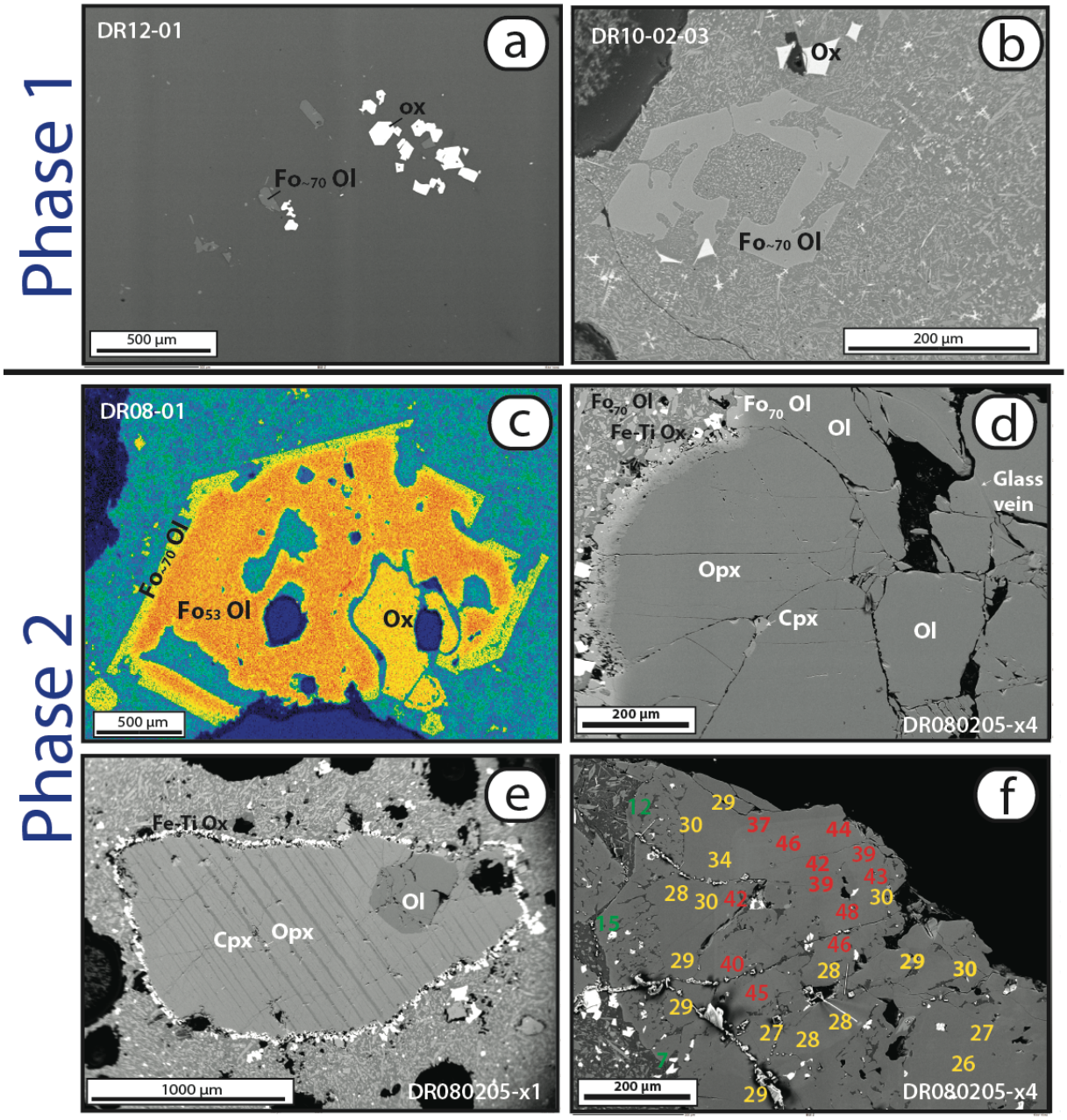

826

827 **Fig. 4**. Petrographic features of the dredged lavas. a) All lavas have very low crystallinity: BSE
828 image of 4 – 6% microlites of $Fo_{\sim 70}$ olivine ($Fo_{\sim 70}$ Ol, Suppl. material Table 4) and
829 titanomagnetite (Ox) in glassy matrix of sample DR1201. b) Many crystals show textures
830 typical of fast growth like these skeletal Fo_{70} olivine and titanomagnetite crystals in fine-grained
831 groundmass (sample DR100203) c) Olivine crystals in late erupted lavas (DR08; DR11) have

low-Fo composition (Fo_{53}) and show reverse zoning (MnO element map); these crystals are associated with large titanomagnetite crystals (ox). d) Harzburgite mantle xenolith from the later erupted lavas (sample DR080205-x4) composed of Fo_{90} olivine and $Mg\#_{90}$ orthopyroxene (Opx); $Mg\#_{90-93}$ clinopyroxenes (Cpx) are associated with SiO_2 and K_2O-rich veins. e) Another mantle xenolith composed of a single crystal of Cpx with Opx exsolutions (sample DR080205-x1) and a few olivine and Opx crystals. f) Zoned clinopyroxene megacryst in sample DR080205-x2. Superimposed colored numbers show estimated depth of crystallization calculated through geobarometry (Putirka, 2008): red numbers are located in the low- Mg# core, yellow: high-Mg# inner rim, green: dendritic outer rim.

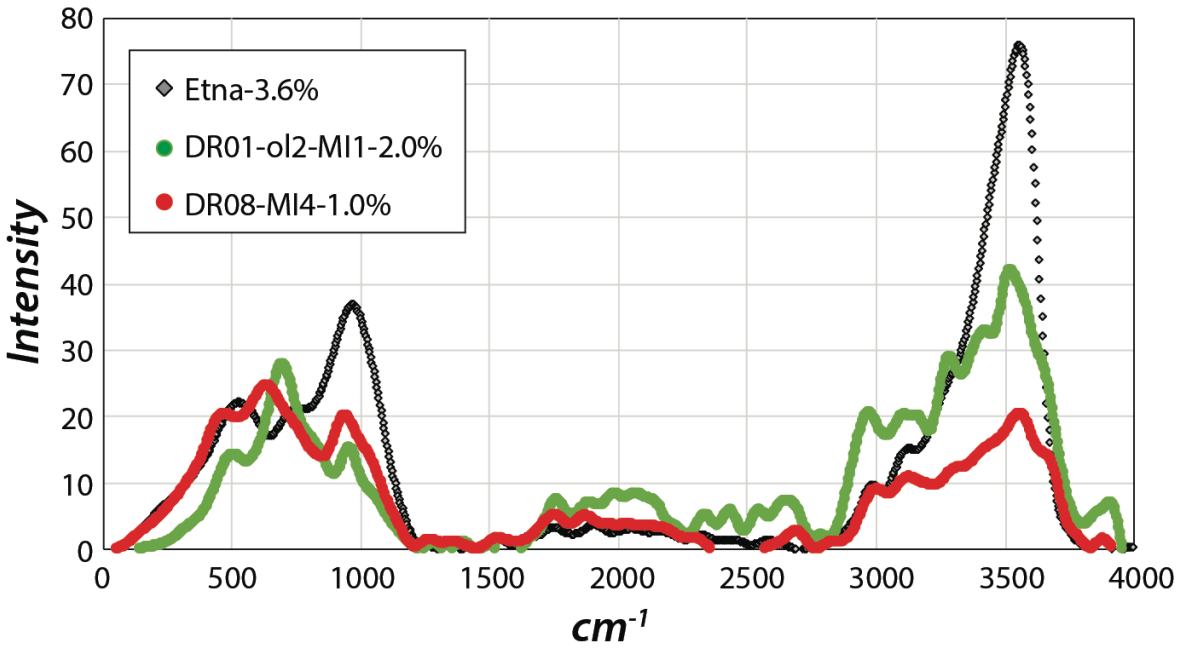

ID	DR1-03-ol2-FI1	DR1-03-ol2-MI1	DR1-03-ol3-emb	DR1-03-ol4-MI	DR8-01-MI1	DR8-01-MI2	DR8-01-MI3	DR8-01-MI4
Glass	melt inclusion	melt inclusion	embayment	melt inclusion	melt inclusion	melt inclusion	melt inclusion	melt inclusion
Host	olivine	olivine	olivine	olivine	spinel	spinel	spinel	spinel
H2O	2.0	0.6	2.2	2.3	1.2	1.0	1.1	1.0

Fig. 5 Raman spectra of an olivine-hosted melt inclusion from sample DR0103 and a spinel-hosted melt inclusion from sample DR0801 compared with reference basaltic glass containing 3.6 wt% of dissolved water (Etna glass). Bands in the 100-1200 cm^{-1} region are related to vibrations of the glass network, while the band at 3570 cm^{-1} is produced by stretching of OH

bonds and its intensity linearly correlates with the concentration in total dissolved water (Di Muro et al., 2006). Table shows H_2O content (wt%) in melt inclusions and embayment in DR0103 and DR0801 samples.

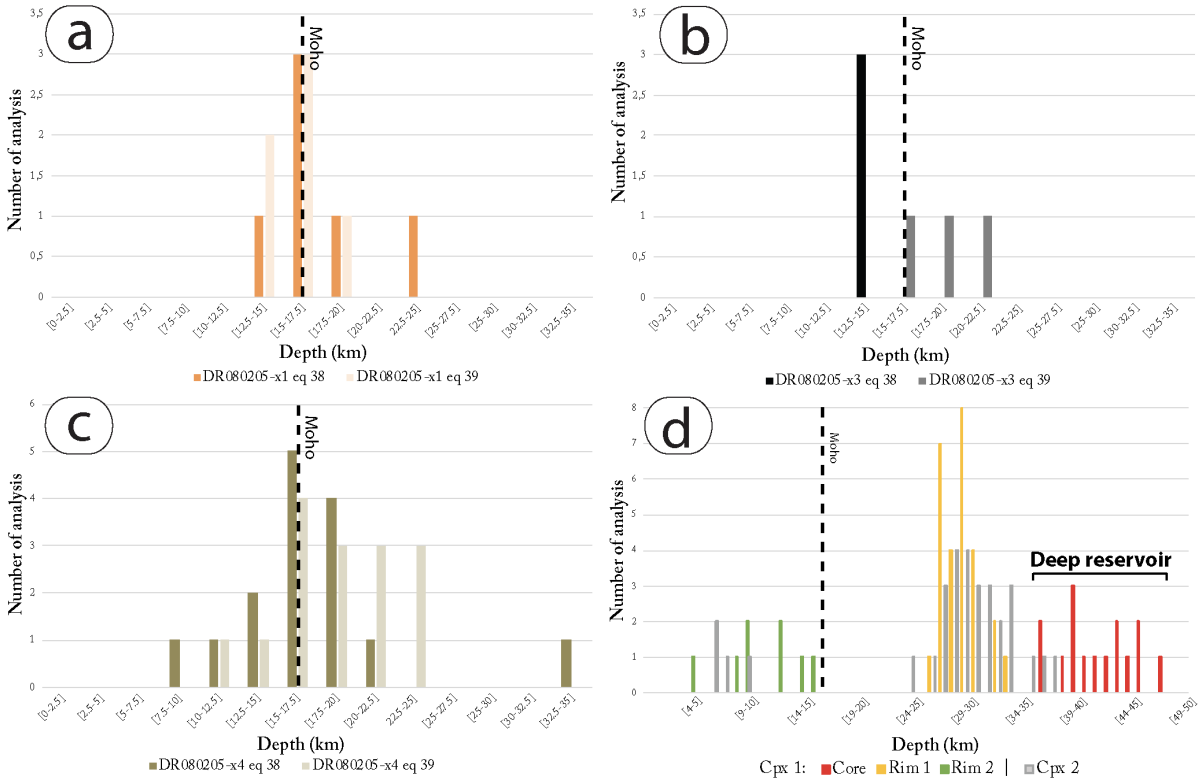

Fig. 6: Histograms showing depth obtained using geobarometry on clinopyroxene-orthopyroxene pairs in the mantle xenoliths in the June 2019 lava flow (DR08). The different colored bars represent results from using different equations (see discussion in text). Pyroxenes located in the three mantle xenoliths (Fig. 4d, e) were equilibrated at pressures of 0.43 ± 0.19 GPa, near the depth of the Moho at 15 – 18 km (black dashed line). (a) DR080205-x1, 0.41 ± 0.19 GPa, (b) DR080205-x3 and 0.46 ± 0.19 GPa (c) DR080205-x4; d) We obtained two additional clusters of pressures of 1.01 – 1.34 GPa and 0.62 – 0.92 GPa with a second set of geobarometry estimations using zoned clinopyroxene megacrysts (Fig. 4f). Moho is shown by a black dotted line (Dofal et al., 2018).

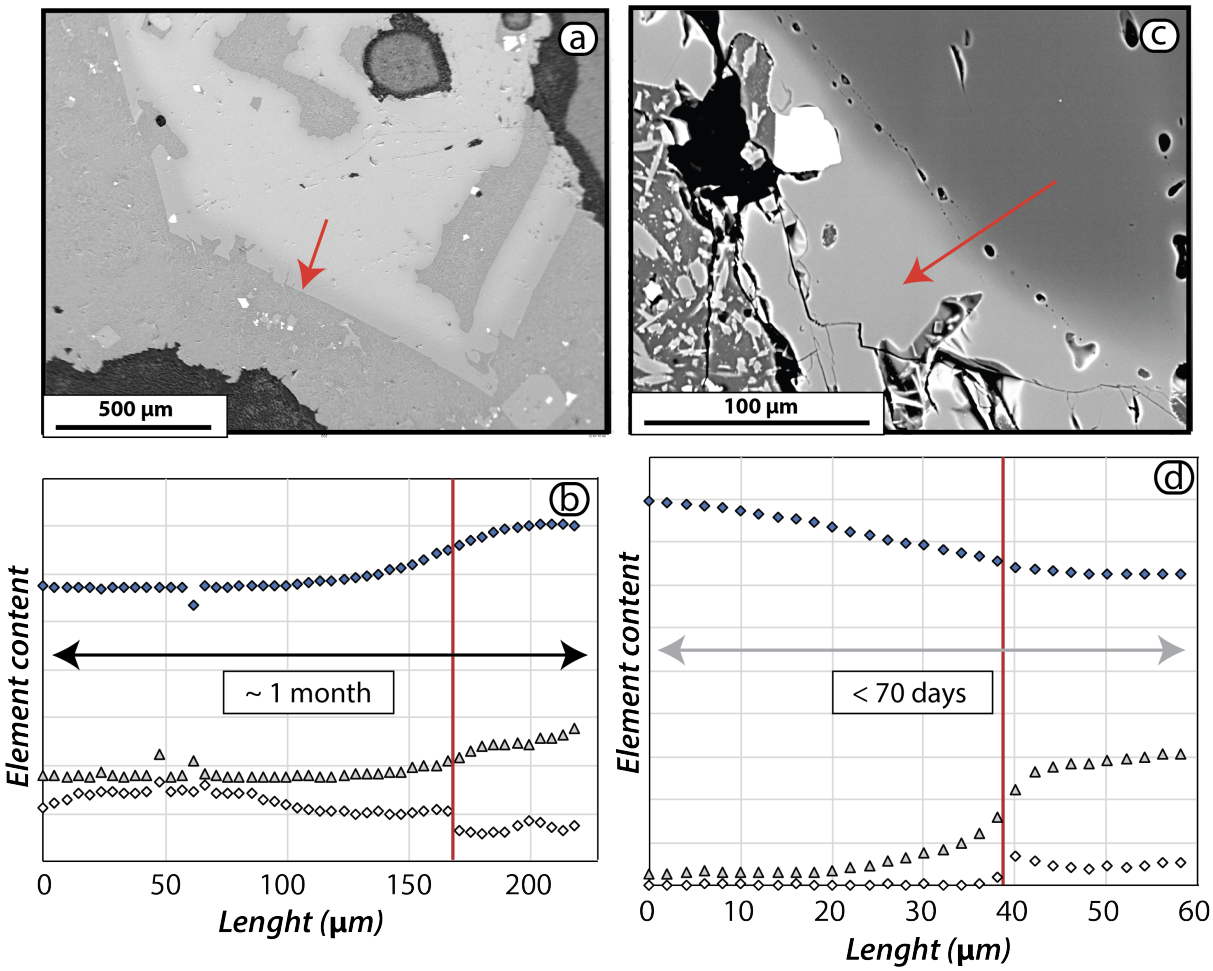

Fig. 7: Core-rim diffusion profiles in zoned olivines. Red arrows show the trace of the profiles on BSE images of a) a reversely-zoned olivine in the DR0801b ALF sample, and c) a normally zoned olivine in the xenolith from the DR080205x4 sample. b) and d) shows Fo, CaO and P_2O_5 core-rim profiles corresponding to the traces presented in a) and c) (Suppl. material Table 6). The diffusion rate for P in olivine is extremely slow so this immobile element marks the initial boundaries between zones that crystallized at different times. In the reversely-zoned phenocryst of b), the initial profile was a step between a Fo_{53} core and a Fo_{70} rim, then Ca and Mg/Fe diffused away from this initial step. In the normally zoned xenolith of d), the initial profile was a step between a Fo_{90} core and a Fo_{72} rim, then Ca and Mg/Fe diffused away from this initial step.

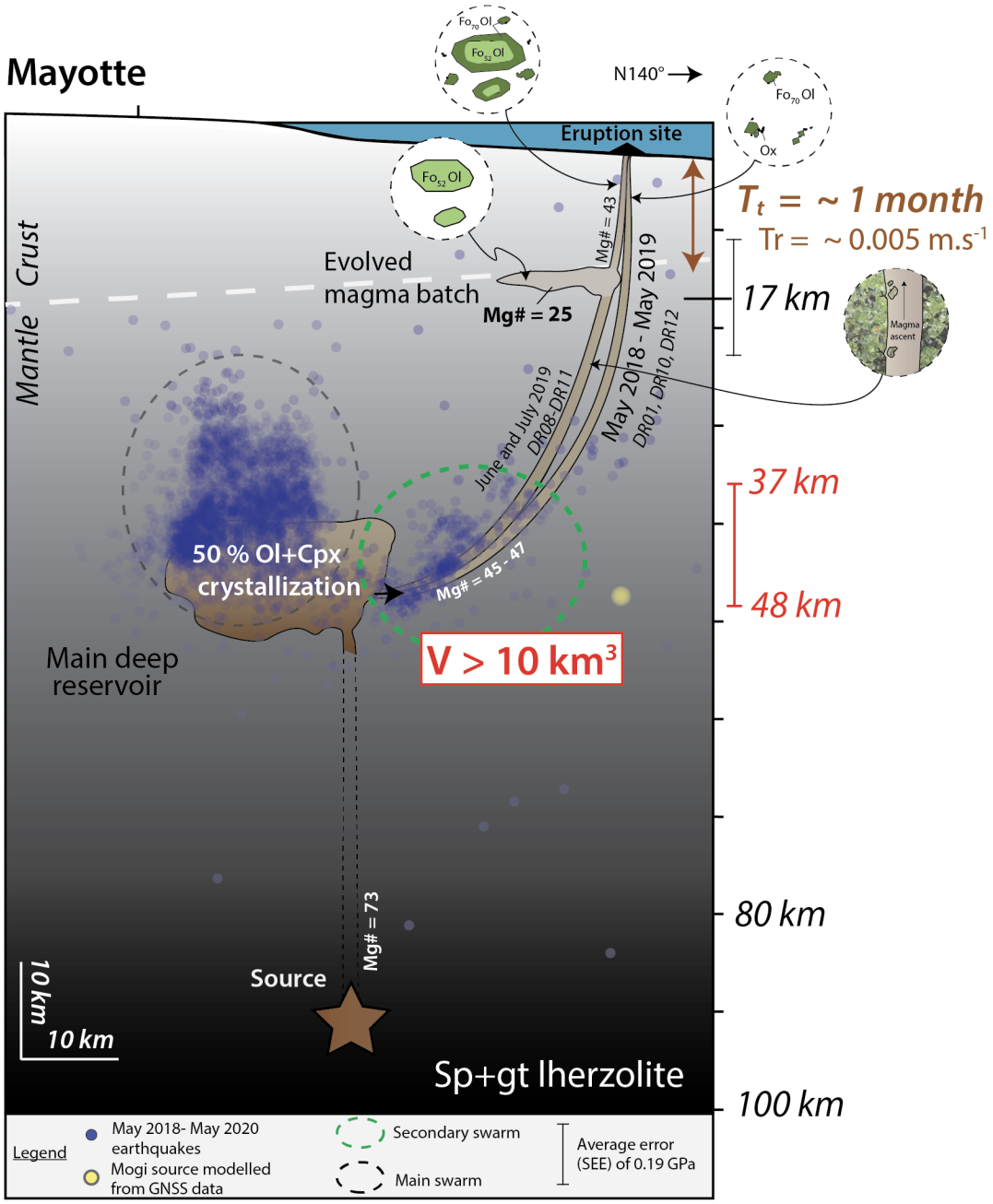

Fig. 8. Magma plumbing system feeding the 2018-2020 Mayotte eruption interpreted on the basis of petrological and geophysical data. Magma produced by partial melting of a spinel (sp) + garnet (gt) lherzolite mantle source undergoes 50% of crystallization (80% cpx + 20% ol) in a large and ≥ 37 km deep magma reservoir with a volume ≥ 10 km^3. Depth of this main deep storage unit constrained by barometric data is in excellent agreement with seismicity location (blue dots, ReVoSiMa, 2021) and geodetic model (yellow dot). Starting from the main deep

reservoir, the magma path evolved during the eruption. During the first year, eruption is fed by direct ascent of magma from the deep reservoir to the surface through NW-SE lithospheric structures. The shape and the size of microlites indicate that most micro-crystallization occurred in the shallow part of the ascending dyke. A shallower and smaller differentiated magma reservoir located close to the Moho (< 17 ± 6 km) was sampled *en route* during the second year of the eruption. It is important to note that this magma batch and the shallow conduit were not imaged by on-land seismometers because they are located too far from the eruption site to allow identification of small, shallow earthquakes. Moho: grey dotted line (Dofal et al., 2018). Tt: Transfer time, Tr: Transfer rate = distance / transfer time, V: volume.

Table captions

Dredges	*Oceanographic cruise*	*DOI : 10.18142/291*	Start dredging			End dredging		
			Latitude	*Longitude*	*Depth*	*Latitude*	*Longitude*	*Depth*
DR01	MAYOBS 1	10.17600/18001217	12°54.30' S	45°43.13' E	3050 m	12°54.51' S	45°43.08' E	2820 m
DR08	MAYOBS 2	10.17600/18001222	12°56.46' S	45°42.88' E	3072 m	12°56.05' S	45°41.91' E	3050 m
DR10	MAYOBS 4	10.17600/18001238	12° 54.94' S	45° 43.31' E	3120 m	12° 55.05' S	45°43.24' E	2950 m
DR11	MAYOBS 4	10.17600/18001238	12°54.80' S	45°41.57' E	3250 m	12°55.20' S	45°41.55' E	3228 m
DR12	MAYOBS 4	10.17600/18001238	12°52.90' S	45°42.94' E	3245 m	12°52.97' S	45°42.93' E	3200 m

Tab. 1: Location of dredges performed during MAYOBS 1 (DR01), MAYOBS 2 (DR08) and MAYOBS 4 (DR10, DR11 and DR12) oceanographic campaigns. No dredges were performed during MAYOBS 3.